https://doi.org/10.1016/j.cej.2022.139390

From Lab to Practical: An ammonia-powered Fuel Cell Electric Golf Cart System

Lingling Zhai[a, b, 1], Chiu Shek Wong[a, b, 1], Honglei Zhang[a, b], Pei Xiong[a], Xiangdang Xue[b], Yiu Lun Ho[b], Cuidong Xu[b], Yat Chi Fong[b], Jie Mei[b], Wing Wa Chan[b], Shu Chuen Ip[b], Shuangxia Niu[b], Shu Ping Lau[a, *], Ka Wai Eric Cheng[b, *], Molly Meng-Jung Li[a, *]

a Department of Applied Physics, The Hong Kong Polytechnic University, Hung Hom, Hong Kong, China

b Department of Electrical Engineering, The Hong Kong Polytechnic University, Hung Hom, Hong Kong, China

* Corresponding author.

Department of Applied Physics, The Hong Kong Polytechnic University, Hung Hom, Hong Kong, China. Email: molly.li@polyu.edu.hk, daniel.lau@polyu.edu.hk

Department of Electrical Engineering, The Hong Kong Polytechnic University, Hung Hom, Hong Kong, China. Email: eric-cheng.cheng@polyu.edu.hk

1 These authors contributed equally.

Abstract

Ammonia (NH_3) is a carbon-free hydrogen (H_2) carrier because it enables liquid-phase H_2 storage and transport under mild conditions. Although the concept of NH_3-to-H_2 has been frequently proposed, the practical application of NH_3 as the energy source for H_2 power automotive systems is rarely reported. In this work, an NH_3-powered fuel cell electric golf cart system was developed and demonstrated as a proof of concept for NH_3-powered fuel cell vehicles. The integration of NH_3 cracker (installed with catalyst), gas purifier, fuel cell, and energy management system formed a successful powertrain that thrusts a golf cart into motion. The catalytic performance of both nickel (Ni) and iron (Fe)-based catalysts was measured, and the optimal catalyst demonstrated a > 99.9% NH_3 conversion at 600 ℃. The gas purifier was confirmed to be capable of removing the residual NH_3 for a proton exchange membrane fuel cell (PEMFC). The fuel cell, when powered by the cracked and purified gas mixture, revealed comparable performance and power output as compared with the pre-mixed fuel gas mixture (75%H_2/25%N_2), demonstrating the feasibility of the whole system. The integration can successfully power 300 and 600 W fuel cells and continuously charge the energy storage system, offering sufficient energy for a 3-kW golf cart for more than 500 km at 25 km/h. This work is an innovative demonstration of an NH_3-powered fuel cell vehicle system, giving rise to a future reference and inspiration for the practical developments of NH_3-based H_2 fuel applications.

Keywords: ammonia decomposition, heterogeneous catalyst, hydrogen carrier, fuel cell, zero carbon fuel.

1. Introduction

To meet the goal of net-zero carbon footprints, H_2 is considered one of the most promising renewable energy sources due to its elemental abundance and zero-carbon emission property. However, it is highly flammable and is the lightest of all the elements (volumetric energy density is only 2.97 Wh L^{-1} at 0 °C, 1 atm) [1]. The on-board H_2 storage and utilization system for automotive applications are largely impeded by low volumetric energy density and safety concerns of H_2. Thus, alternative H_2 carriers are indispensable to achieving cost-effective and efficient H_2 storage and transportation. Recently, NH_3, a carbon-free H_2 carrier, is emerging as a promising clean energy alternative because of its high H_2 density (17.8 wt%), easier liquidation, and safer storage. The volumetric energy density of NH_3 is as high as 2916.7 Wh L^{-1} at room temperature and at low pressure of ca. 8 bar, which is more than double that of compressed H_2 at 700 bar (1388.9 Wh L^{-1}) [2]. Therefore, NH_3 has been considered by many developed countries as a key enabler for a green H_2 economy [3-5].

Generally, the utilization of NH_3 as an energy carrier can be divided into two approaches: (i) direct utilization and (ii) indirect NH_3 fuel cells. The direct utilization involves NH_3 combustion and fuel cell technologies, such as NH_3-fed solid oxide fuel cell (SOFC), alkaline NH_3 fuel cells (AFC), membrane-based NH_3 fuel cells, etc. However, the direct NH_3 fuel cells suffer either from high operation temperatures (> 800 ℃ for SOFC) or carbonate generation issues (e.g., AFC), hence lowering the performance [6]. On the other side, converting NH_3 into H_2 via the thermochemical route (indirect route) is considered more practical: The dehydrogenation of NH_3 generates nitrogen (N_2) and H_2 gas mixture ($2NH_3 \rightarrow N_2 + 3H_2$), which can be used directly as a fuel to power existing fuel cell systems.

Hence the method of NH_3 cracking for the on-site generation of H_2 for fuel cells has been widely proposed [7-9].

Large amounts of literature precedents have reported active NH_3 cracking catalysts while mostly in lab-scale (catalyst <1g), such as Ru/γ-Al_2O_3 [10], Ru/MgO [11], Ni/SiO_2 [12] and FeCo/CNT [13]. Some inspiring works also demonstrated the design and realization of NH_3-to-H_2 fuel technology. For example, Yoon's group designed a 1 kW H_2 powerpack equipped with an isobutane-fueled heating furnace. The testing and verification of NH_3 conversion was conducted in 0.6 g Ru/La-Al_2O_3 catalyst and showed stability for more than 2 h, which was also successfully demonstrated on tethered drone application [1]. Although this powerpack is not entirely carbon-free due to the furnace fuel emissions, the concept and system design enabled the progress of portable and on-demand H_2 production via NH_3 as a medium. On the other hand, stationary NH_3-to-H_2 applications have also been presented, demonstrating energetic and economic performance. Examples can be found in the indirect NH_3 fuel cell system powering 10 kW electricity [14], the WE-NET project to crack NH_3 at 142.8 ton/h and supply H_2 at 17.6 ton/h [3], and the NH_3-to-H_2 plant operated at a thermal efficiency of 68.5% to produce 200 metric tons per day of pure H_2 [15].

Although many excellent precedents have proved the feasibility of the NH_3-to-H_2 idea, portable and on-board NH_3-powered fuel cell automobile systems have not been realised on a practically viable scale. In this work, an NH_3-powered fuel cell electric golf cart system was developed and demonstrated as a proof-of-concept for NH_3-powered fuel cell vehicles. The NH_3-fuel cell system contains three main parts: cracking catalyst, energy conversion platform, and energy management unit. By optimising commercial catalyst materials and energy conversion apparatus, the developed integration demonstrated its

ability to continuously supply H_2 energy at high efficiency under exergonic and CO_x-free conditions. Equipped with a standard size NH_3 cylinder containing 10 kg NH_3, the NH_3-to-H_2 system can successfully power 300/600 W fuel cells and continuously charge the energy storage system mediated by a dedicatedly designed energy management unit, providing sufficient energy to drive a 3 kW golf cart for more than 500 km at a speed of 25 km/h (details in Supporting Information). This work provides the first on-board NH_3-powered fuel cell vehicle at a practical scale with high stability and efficiency. Furthermore, the material optimization and energy system integration can offer new insights for NH_3-to-H_2 process design, and, most importantly, this development can help close the gap between NH_3 supply and H_2 utilization, as shown in **Fig. 1**.

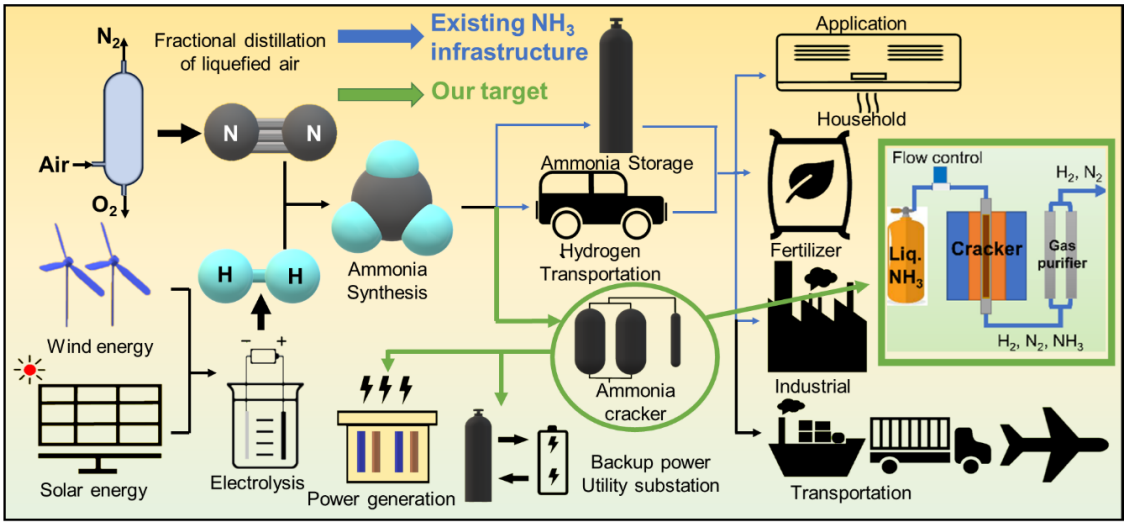

Fig. 1. Schematic diagram of NH_3-based infrastructure for fuels and fertilizers.

2. Experimental section

2.1 Reagents and materials

Commercial catalysts denoted Ni-HD, Fe-HD and Fe-BZ were purchased from Suzhou Hengda Purification Equipment Co., LTD (HD) and Qinghe Bozuan Metal Materials Co. , LTD (BZ), respectively. 13X and 5A zeolites were purchased from Nankai University. The proton membrane exchange fuel cells (PEMFCs) were purchased from Suzhou Sinero Technology., Ltd. Ruthenium chloride ($RuCl_3$) was purchased from Energy Chemical and used as received. Sulphuric acid (H_2SO_4) solution and sodium hydroxide (NaOH) were purchased from Sigma-Aldrich.

2.2 Pretreatment of Ni-HD and Fe-HD

The commercial catalysts were grinded and sieved with different sieve opening sizes ranging from 18-80 meshes.

2.3 Preparation of Ru-doped Ni-based catalyst (Ru-Ni-HD)

A precursor solution was prepared by dissolving 0.1 M $RuCl_3$ in ethanol under vigorous stir to get a homogeneous solution. Then 100 g of Ni-HD (45-60 mesh) was immersed into $RuCl_3$ solution (0.1 M) for overnight. Then the mixture was filtrated and placed in a vacuum oven at 95 °C for 24h. After dried, the sample was placed at the center of a tube furnace and calcined at 550 °C under 5% H_2 atmosphere for 4 h.

2.4 Catalytic performance characterization

For the catalytic performance testing, the catalysts were sieved into 45-60 meshes and placed into a 316L 1 inchstainless-steel tube, the stainless-steel tube is located in the centre

of a temperature controlled electrically heated furnace. The total volume of the catalysts ranges from 50 to 180 mL, which depends on the specific testing parameters. High purity ammonia gas (≥99.99%) then passed through the catalyst tube and controlled by a mass flow controller (D6341, Bronkhorst). For both activation and reaction process, the reactions were performed under atmospheric pressure. The concentrations of different components, i.e., NH_3, H_2, N_2, in the outlet gas were measured by a titrator (Orion Star™ T900, Thermo Fisher Scientific) and a mass spectrometer (MS, HPR-20 EGA, Hiden), which was equipped with a quadrupole probe and a secondary electron multiplier (SEM) detector (850 eV). Caution that NH_3 gas is highly caustic and hazardous, all NH_3 decomposition components (gas regulator, mass flow controller, gas purifier, pipes etc.) should be corrosion resistant. To safely handle ammonia and the produced hydrogen as a fuel, spaces containing fuel lines should be equipped with ammonia and hydrogen sensors combined with good ventilation. As ammonia exposure to humans and the environment should be limited as much as possible, in case of ammonia/hydrogen leakages, the tank and fuel lines should be designed to have remotely operated shut-off valves to isolate the leakage and limit its impact.

For a typical titration analysis, 200 mL 0.1 mol L^{-1} H_2SO_4 solution was used to trap the unreacted NH_3 in the exhaust gas for 5 minutes. After that, 20 mL of the absorbant was taken out by pipette to perform back titration against 0.12 mol L^{-1} NaOH solution. The reaction between H_2SO_4 and NaOH is given by Eq. (1):

$$H_2SO_4 + 2\mathrm{NaOH} \rightarrow \mathrm{Na_2SO_4} + 2H_2O \quad (1)$$

Therefore, the number of reacted moles of H_2SO_4 $\left(n_{\mathrm{H_2SO_4}}\right)$ can be calculated by Eq. (2):

$$n_{H_2SO_4} = \frac{1}{2} \times M_{NaOH} \times V_{NaOH} \quad (2)$$

where M_{NaOH} is the concentration of NaOH and V_{NaOH} is the volume of NaOH consumed in the titration analysis.

The number of moles of H_2SO_4 reacted with NaOH can further be used to calculate the number of moles of ammonia n_{NH_3} trapped in the 20 mL H_2SO_4 solution, see Eq. (3):

$$n_{NH_3} = 2 \times \left(M_{H_2SO_4} \times V_{sample} - n_{H_2SO_4}\right) \quad (3)$$

where $M_{H_2SO_4}$ is the concentration of H_2SO_4 and V_{sample} is the volume of the sample solution.

The total number of moles of ammonia N_{NH_3} trapped in the 200 mL H_2SO_4 solution can then be calculated by Eq. (4):

$$N_{NH_3} = n_{NH_3} \times \frac{V_{total}}{V_{sample}} \quad (4)$$

where V_{total} is the total volume of the H_2SO_4 solution.

Number of moles of ammonia flow through the catalyst N_{inlet} during the collection time is given by Eq. (5):

$$N_{inlet} = \frac{1}{24} \times f_{NH_3} \times t_{collect} \quad (5)$$

f_{NH_3} is the ammonia flow rate and $t_{collect}$ is the duration of the output gas collection.

Therefore, the conversion rate X of the tested catalyst can then be given by Eq. (6):

$$X = \frac{N_{\text{inlet}} - N_{\text{NH}_3}}{N_{\text{inlet}}} \times 100\% \quad (6)$$

For the mass spectrometer, 50 mL of the exhaust gas was transferred to the mass spectrometer, and the gas component amount and the corresponding concentration were accordingly analyzed. The NH_3 conversion was calculated using Eq. (7):

$$\text{NH}_3\ conversion\ = \frac{1 - [\text{NH}_3]_{outlet}}{1 + [\text{NH}_3]_{outlet}} \times 100\% \quad (7)$$

where $[NH_3]$outlet refers to the measured volume of NH_3 flowing out of the reactor.

2.5 Fuel cell testing

The performance of the fuel cell at different conditions (gas combinations/catalysts) was evaluated by assessing the electrical output characteristic. The fuel cell stack was fed with either a gas mixture (75%H_2/25%N_2) or NH_3 decomposed gas at ambient temperature without humidification, and the start-up time was ~2 seconds. The electrical output terminals of the fuel cell stack were connected to drive a programmable electronic load (Elektro-automatik EA-EL 9050-510) which was set to constant current (CC) mode. The voltage across the output terminals was monitored. Input gas was supplied to the fuel cell at pressures between 0.45 to 0.6 bar gauge, the output voltage of the fuel cell was observed under no-load condition, and the voltage at steady-state was measured. It should be noted that, since hydrogen is highly flammable, the hydrogen gas sensors should be set aside to monitor the ambient H_2 concentration, and the testing should be conducted in a fume hood or open air with good ventilation. The CC setting at the electronic load was increased gradually at the steps of 1 A. The steady-state output voltage of the fuel cell at different load current settings was recorded. The output power was calculated by Eq. (8):

$$W = UI \quad (8)$$

Where U was the steady-state output voltage and I was the corresponding current.

2.6 Material characterization

Powder X-ray diffraction (XRD) measurement was conducted on a Rigaku Smartlab X-ray diffractometer using Cu Kα radiation (λ = 1.5418 Å) at 45 kV and 200 mA. The XRD patterns were indexed and quantitatively analyzed according to the ICDD PDF-4 database. The morphology and microstructure of samples were investigated by scanning electron microscope (SEM) using a Tescan VEGA3 microscope. Nitrogen adsorption-desorption measurements were conducted on a Micrometrics ASAP2020 instrument at 77K. Transmission electron microscopy (TEM), high-angle annular dark-field scanning transmission electron microscopy (HAADF-STEM) and energy dispersive X-ray (EDX) mapping were carried out on a JEOL JEM-2100F at 200kV, using the holey carbon-coated copper grid. Inductively Coupled Plasma Optical Emission Spectroscopy (ICP-OES) characterization was performed on an Agilent Varian 720ES equipment.

3. Results and discussion

3.1 The catalysts

Various metal/metal oxide catalysts (Ni, Fe, Ru, Co, Mo) have been exploited to decompose NH_3. From the literature precedents [16-18], a volcano relationship between the turnover frequency (TOF) of NH_3 decomposition and nitrogen binding energy was revealed in different metal-based catalyst systems. That means, too strong metal-nitrogen (M-N) bonding results in difficult nitrogen desorption from the surface of the catalyst (N poisoning). In contrast, too weak M-N bonding makes the catalyst inactive for N-H

dissociation. Ru catalyst has been identified as the most active NH_3 decomposition catalyst at low reaction temperatures (450 to 550 ^oC) due to its moderate binding strength to nitrogen [19, 20]. However, the commercial opportunity of Ru as an NH_3 decomposition catalyst has been limited due to its high cost and scarcity. This study aims for a practical application that needs large amounts of catalyst (at least hundreds of grams to a few kilograms) from an easy and large-scale synthesis process. Therefore, the high cost of precious Ru would lead to budget concerns. Given that the commercial Ni or Fe-based catalyst has been widely adopted in the NH_3 decomposition units for the semiconductor industry [21], metallurgy [22], and other industries [23] or scientific research [24] that require an inert gas and H_2 gas atmosphere, we choose Ni or Fe-derived catalysts to be used in our proof-of-concept prototype.

In this research, cost-effective, facile, and industrially viable catalyst preparation strategies have been implemented to meet the goal of practical vehicle application (see details in Supporting Information). Three commercially available catalyst precursor materials, denoted as Ni-HD, Fe-HD and Fe-BZ, were used (see **Table 1** and Supporting Information). A Ru modified Ni-HD catalyst was also presented as an initial trial. Some material treatments have been conducted to construct a low-cost and stable cracking catalyst and ensure good NH_3 cracking efficiency.

Table 1 List of the catalyst precursor materials.

Catalyst	Ni-based catalyst	Fe-based catalyst #1	Fe-based catalyst #2

Label	Ni-HD	Fe-HD	Fe-BZ
Shape	shaped cylindrical shape	shaped cylindrical shape	granular
Size/mm	15× 15 × 25	15 × 15 × 25	45 – 60 mesh
Pretreatment	crush into 45-60 mesh	crush into 45-60 mesh	use directly
Composition	40 wt.% NiO + 60 wt.% Al_2O_3	Fe_3O_4	Fe_3O_4

226

227 To analyze the crystallographic structure and phase purity, all samples were examined by
228 XRD. As shown in **Fig. 2**a, the Ni-HD and Ru-Ni-HD reveal similar XRD patterns, where
229 the peaks locate at 35.1°, 37.8° and 43.4°, corresponding to (104), (110) and (113) planes
230 of Al_2O_3 (JCPDS 10-0173). The peaks located at 18.1° and 25.5° can be ascribed to (001)
231 and (100) planes of the binary alloy Al_3Ni_2 (JCPDS 65-9699), and the peak located at 44.4°
232 belongs to (111) plane of Ni (JCPDS 65-0380). No obvious peak of Ru was detected, which
233 is probably due to the low concentration (c.a. 2 wt%) and small size of Ru clusters.
234 Therefore, it is concluded that the Ni-HD catalyst contains mixed phases of Ni and Al_3Ni_2
235 loaded on Al_2O_3, and Ru species in the Ru-Ni-HD sample are dispersed on the Ni-HD
236 matrix. On the other hand, for the XRD spectra of Fe-HD and Fe-BZ, the characteristic
237 peaks match well with Fe_3O_4 (JCPDS 65-3107). As shown in **Fig. S1**, the peaks at 30.1°,
238 35.5° and 43.1° present (220), (311) and (400) planes of Fe_3O_4, respectively. Moreover,
239 the specific surface area, pore volume and pore diameter of the above-mentioned catalysts
240 were determined by nitrogen adsorption-desorption measurements based on a Brunauer-
241 Emmett-Teller (BET) instrument, as shown in **Table 2** and **Fig. S2**. The surface area of Ni-

242 HD was measured to be 101.5 m^2/g, which is ten times larger than Fe-based catalysts,
243 indicating a larger number of catalytic sites available for reaction. The pore size
244 distributions (**Fig. S3)** of Ru-Ni-HD and Ni-HD show no obvious difference, indicating
245 that the pore structures were well reserved after Ru doping, and the pore sizes in both
246 catalysts are of mesoscale. ICP-OES characterization indicated that the Ru content in bulk
247 Ru-Ni-HD was determined to be ca. 1.96 wt%, matching well with the nominal weight
248 loading of Ru (2 wt%).

249 The morphology of the catalysts was characterized by SEM as shown in **Fig. 2**b-e. After
250 downsizing (via a grinder) and sieving into 45-60 mesh, the Ni-HD particle reveals a
251 smooth surface with a diameter of ~ 300 μm. With the doping of Ru on the catalyst surface,
252 the Ru-Ni-HD particle shows a relatively rough surface, presumably due to the surface
253 roughening during the metal loading and the subsequent heat treatment processes. As for
254 the Fe-based catalyst precursors, Fe-BZ shows a dense morphology without any pore or
255 wrinkle, whereas Fe-HD presents a rough surface with tiny grains attached owing to the
256 downsizing and sieving treatments. The catalysts reveal distinctly different morphologies
257 with similar particle sizes of 45-60 mesh. To reveal the elemental composition of the Ni-
258 based catalysts, EDX spectroscopy was conducted through SEM. As illustrated in **Fig. S4**,
259 the Ni-HD catalyst shows uniform distributions of O, Al and Ni. After Ru modification,
260 the relevant elements of Ru-Ni-HD catalyst (**Fig. S5**) remain in uniform distributions. The
261 corresponding SEM-EDX spectra and elemental ratios are given in **Fig. S6** and **Table S1**.
262 To further confirm the dispersion of Ru in nano-scale, TEM and the EDX mapping under
263 HAADF-STEM mode were conducted. As shown in **Fig. 3**a-e, all elements are evenly
264 dispersed. The particle sizes are around 6-7 nm as found in the high-resolution TEM

(HRTEM, **Fig. 3**f), where the inset shows one particle with resolved lattice distance of 2.1 Å, matching well with the (101) plane of Ru.

Table 2 BET analysis of Ni and Fe-derived catalysts. The pore size and diameter analysis of Fe-BZ is not applicable due to the low surface area.

	Surface area (m^2/g)	Pore volume (cm^3/g)	Pore diameter (Å)
Ni-HD	101.5	0.16	63.6
Ru-Ni-HD	101.1	0.19	76.5
Fe-BZ	1.3	NA	NA
Fe-HD	3.3	0.01	154.1

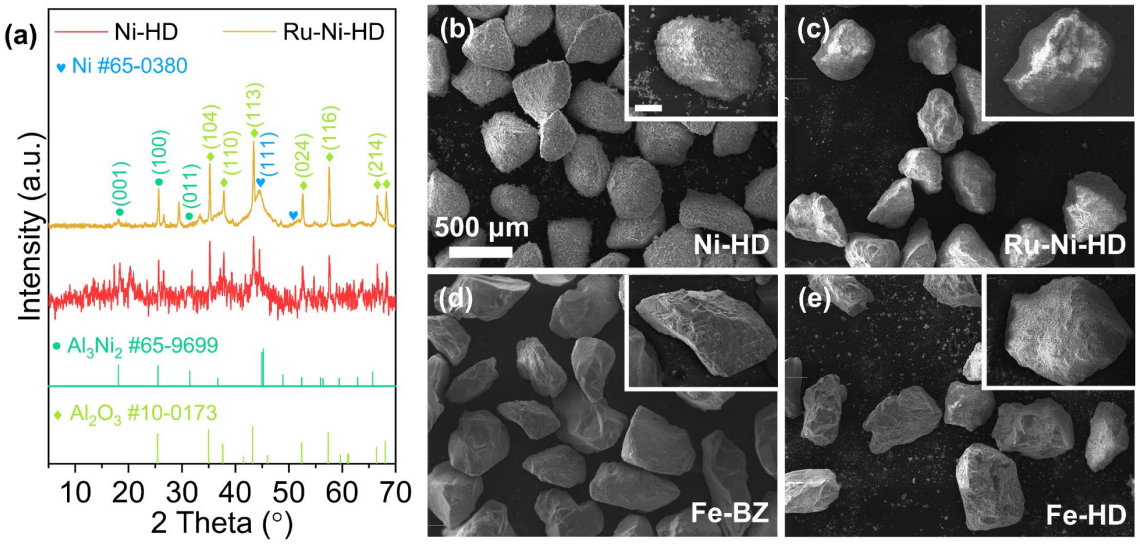

Fig. 2 (a) XRD spectra of as-prepared catalysts. SEM images of (b) Ni-HD, (c) Ru-Ni-HD, (d) Fe-BZ and (e) Fe-HD. Inset shows enlarged images of individual particles with a scale bar of 100 μm.

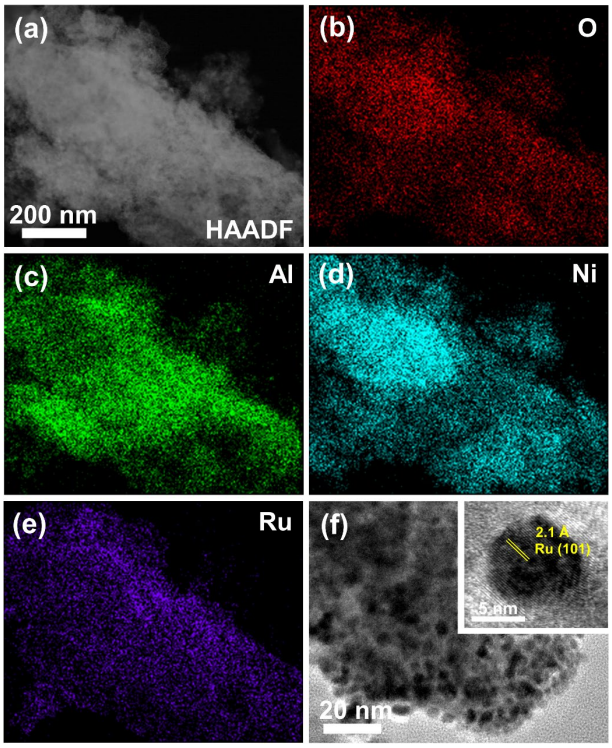

Fig. 3 (a) HAADF-STEM image of Ru-Ni-HD. EDX elemental mapping of (b) O, (c) Al, (d) Ni and (e) Ru. (f) HRTEM image of dispersed Ru-Ni-HD nanoparticles. The inset shows an enlarged image of one Ru particle with (101) plane.

3.2 Catalytic performance

The catalytic performance of all catalysts was performed in a fixed-bed cylindrical flow reactor under different temperatures (450 to 750 ℃). Particle size ranges from 15 to 60 mesh and gas flow rate varies from 200 to 4,000 mL/min. The catalytic activity was first measured with a particle size of 45-60 mesh under gas hourly space velocity (GHSV) of 3000 $h^{-1,}$ as shown in **Fig. 4**a. The NH_3 conversion efficiency increases with increasing temperature, and the testing result gives the "S" type NH_3 conversion-temperature curves

for all catalysts. The Ru-Ni-HD exhibits the best performance with a high NH_3 conversion of 99.90% at 600 ℃, and the Ni-HD without Ru doping reveals the same high conversion rate at 650 ℃. On the other hand, the Fe-BZ demonstrates the worst activity, and the temperature for Fe-based catalysts to reach a > 99% conversion is as high as 750 ℃. These results demonstrate the satisfactory performance of the commercial Ni-HD catalyst series for potentially practical application.

Generally, the Ru-based catalyst has been reported promising for low-temperature NH_3 decomposition (400~500 ºC, lab-scale testing) [17]. Our initial testing result demonstrates the improved catalytic activity of Ru than that of the non-precious metal catalysts. However, further optimizations are still ongoing to make the Ru catalyst more active (lower temperature) and cost-effective (less Ru loading) to enable it suitable for practical applications. At this stage, when considering the cost incurred by the expensive Ru precursor and its marginal reduction to the energy consumption while lowing the NH_3 decomposition temperature from 650 to 600 ºC, the 2nd highest performing catalyst candidate, i.e., Ni-HD, is the best choice to be used for the proof-of-concept prototype system. Catalyst performance with different GHSV was evaluated and presented in **Table S2**.

Three groups of Ni-HD obtained through different sieve opening sizes are tested to evaluate the effect of particle size, as shown in **Fig. 4**b. The sample with 45-60 mesh demonstrates the best performance, and the worst performance was recorded in the 18-45 mesh size range. The low activity of 18-45 mesh Ni-HD is due to the low packing efficiency and low surface areas of large particles. It is worth noting that when the particle size was reduced to > 60 mesh (250 μm), the reaction tube would be blocked, and the pressure built up in the catalyst

tube lowered the NH_3 conversion. In addition, the > 60 mesh catalyst was plugged totally at 550°C; hence the testing could not be completed at high temperatures. Therefore, Ni-HD with the particle size of 45-60 mesh was chosen as the demonstration catalyst for the NH_3-fuel cell golf cart system.

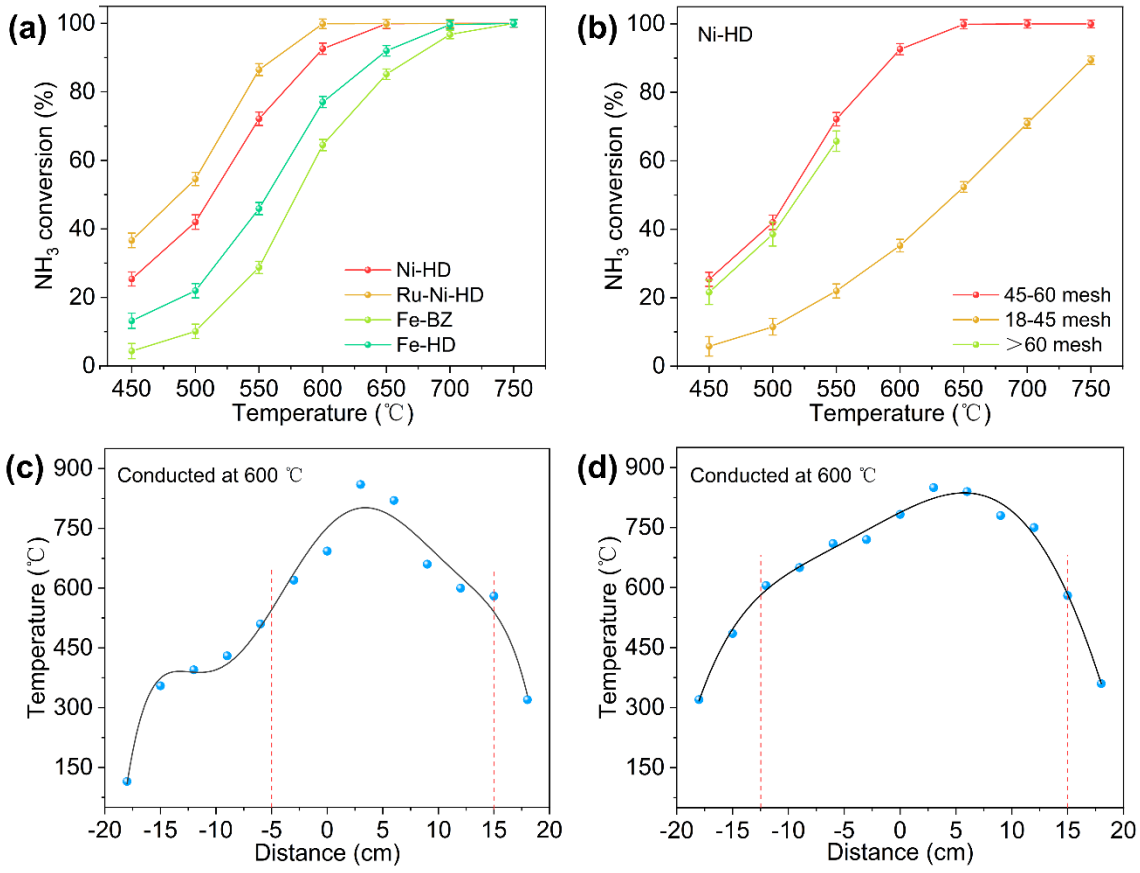

Fig. 4 (a) NH_3 conversion of as-prepared catalysts as a function of temperature with particle sizes of 45-60 mesh at GHSV = 3000 h^{-1}. (b) Catalytic activities of Ni-HD as a function of temperature with different particle sizes range from 18 to 60 mesh. Temperature distributing curve of the furnace as a function of distance from the midpoint (c) before optimization and (d) after optimization.

3.3 Reactor optimization

The scale-up of an NH_3 cracker requires the design and optimization of chemical reacting systems. The engineering design of the catalytic reaction unit is not only influenced by the structure of the packing matrix (shape, dimensions, and the packing density of the catalyst particles), but also the cracker design (furnace size, power rating, insulation, etc.). Conventional packed-bed crackers for H_2 production use shaped catalysts in the form of pellets or cylindrical extrudates. However, heat transfer and mass diffusion are often limited in the catalyst reactor, and significant axial and radial temperature gradients can exist in the catalyst bed, which in turn dramatically lowers the reaction efficiency [25]. At the current prototype scale, the reactor tubes were packed by the catalyst in size-optimized powders to minimize the heat and mass transfer problems. The packed 1-inch stainless steel reaction tubes were wound by the heating coil and fixed at the middle part of the furnace to maximize the heating efficiency. The inlet and outlet sides were sealed with thermal insulation material to minimize heat loss. The furnace chamber was covered by shaped refractory fiber and mounted on a stainless steel rack to have better thermal insulation and minimize the catalyst movements when driving the golf cart. Accordingly, the insulation of the cracker was much improved, as evidenced in **Fig. 4**c-d, where the effective heating zone was greatly enlarged from 20 to 37.5 cm by 187.5%, hence improving the energy efficiency. Besides, the temperature fluctuation of the heat zone was also largely decreased. It should be noted that to make each component in the cracking unit function together, many factors should be carefully considered, such as the coupling between catalytic reactions, heat transfer, fluid mechanics, heating sources, etc., which will serve as future optimization ideas after the current work.

3.4 Gas purification

The systematic investigation of different catalyst components and reactor configuration optimization proves our assembled cracker system. The next step is to purify the output gas before feeding it into a fuel cell. According to ISO14687-2, the fuel gas feed must be <0.1 ppm of the unconverted NH_3 to prevent irreparable damage to a PEMFC [26]. Any residual NH_3 higher than this tolerance level will damage the acidic membrane by forming NH^{4+} ions. The degradation of the membrane significantly reduces proton conductivity and, in turn, deteriorates the efficiency and lifetime of the fuel cell [27, 28]. Several approaches for NH_3 removal were considered in the literature precedents, including liquid acid traps [29] and solid adsorbents such as zeolite molecular sieves [30], activated carbon [31], metal-organic frameworks [32], and metal halides [33]. Zeolites are economically attractive materials and have many advantages as NH_3 adsorbents, such as high adsorption capacity, robustness, and excellent regeneration stability. Here, two types of zeolites were adopted, namely, 13X and 5A. The two zeolites are both in size range of 3-5 mm, with a packing density of ca. 0.65 g/cm^3 and a residual water content lower than 1.5 wt.%. The zeolites were used as adsorbents to reduce the NH_3 concentration in the cracked gas mixture and used as received without further modifications. Dynamic adsorption of the zeolite samples was studied by the specially designed breakthrough testing apparatus, as shown in **Fig. 5**a. The testing apparatus is constructed by two parallel 1-inch stainless steel columns filled with zeolite samples and connected in-line to the reactor outlet or the simulated NH_3 decomposition gas as indicated in the figure. The simulated decomposed gas was adjusted with a NH_3 concentration of 1000 ppm and confirmed by a mass spectrometer (Hiden Analytical HPR - 20) prior to each test. The breakthrough time and the outlet NH_3 concentration of the adsorption column were measured simultaneously by the trace NH_3

detector (PPM MiniPID2) and the mass spectrometer. As shown in **Fig. 5**b, the concentrations of NH_3 are close to zero for both 13X and 5A zeolites for more than 60 min, showing effective NH_3 purification for PEMFC application. Particularly, it was found that the remained NH_3 concentration after adsorption by 13 X was almost undetectable until the breakpoint of over 100 min. Thus, it is considered that 13X is more suitable for removing residual NH_3 in the output gas. Literature precedents have also shown that dynamic adsorption of NH_3 to below 0.1 ppm could be successfully achieved by commercial X-type faujasite zeolites [34]. Therefore, 13 X zeolite is adopted as the solid adsorbent for NH_3 removal in our NH_3-fuel cell vehicle prototype.

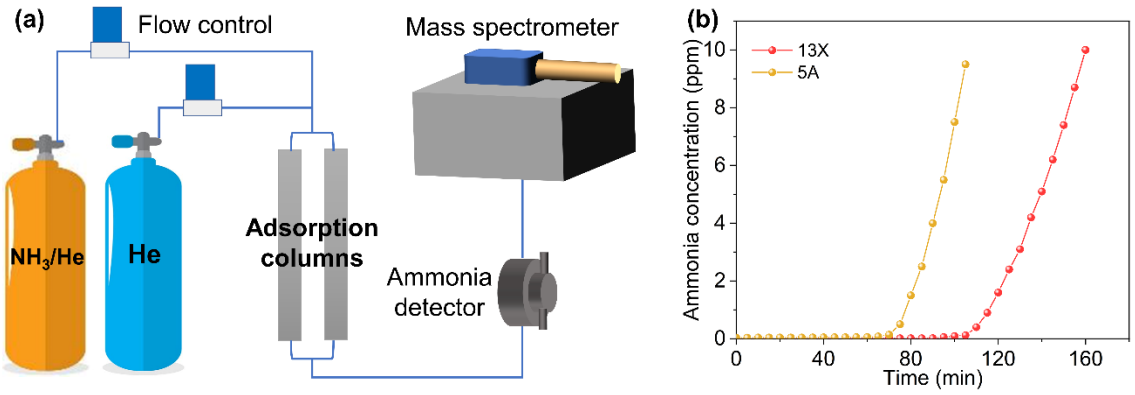

Fig. 5 (a) Dynamic adsorption breakthrough testing apparatus with simulated decomposition gas. The outflowing gas was monitored by mass spectrometer and NH_3 sensor. (b) The breakthrough curve for the NH_3 adsorption process using simulated NH_3 decomposed gas in 13X and 5A zeolites.

3.5 Fuel cell testing

For the NH_3-derived H_2 source (75% H_2 and 25% N_2), a typical dead-end anode operation in a PEMFC would cause the build-up of nitrogen, which will block the active sites towards the dead-ends of the flow field channels (blanketing effect) and impact upon the current generation [35, 36]. To address this issue, fuel cells with custom-made controllers for flow-through operation mode have been configured. In addition, in this study, two kinds of fuel cells (300 W and 600 W, Suzhou Sinero Technology., Ltd., specifications in **Table S3**) were employed and tested under variable system conditions. The mass power density of PEMFCs was 120 W/kg, and the operation pressure was between 0.45 to 0.6 bar. To evaluate the performance of the fuel cell powered by the cracked gas mixture, the 300 W and 600 W fuel cells were tested and monitored under the feeding of a pre-mixed fuel gas mixture (75% H_2/25% N_2). As shown in **Fig. 6**a, under the current range of 0 to 15A, the output power of the 300 W fuel cell increased from 0 to 261.9 W with voltage ranges from 28.0 to 17.5 V, preserving 87.3% of the full rated power.

To further adapt the golf cart's power requirement under variable conditions, another 600 W fuel cell was also investigated. As shown in **Fig. 6**b, the 600W fuel cell delivered a power of 503.8 W at 20 A and 25.2 V with the pre-mixed fuel gas mixture (75% H_2/25% N_2). The satisfactory performance of the fuel cells with simulated cracked gas under a simple flow-through mode demonstrates the feasibility of the whole design. The future optimization will include a modified fuel cell gas-feeding unit with a programmable and flexible gas-purge controller to enhance the fuel cell's performance when fueling with 75% H_2/25% N_2. Furthermore, a fuel cell power conditioning system will be designed and equipped with different power levels for the fuel cell systems. The power conditioning system converts the voltage and power levels output by the fuel cell system to the voltage

and power levels required by the battery pack to charge the Li-ion batteries in an energy controller for optimal power and control management.

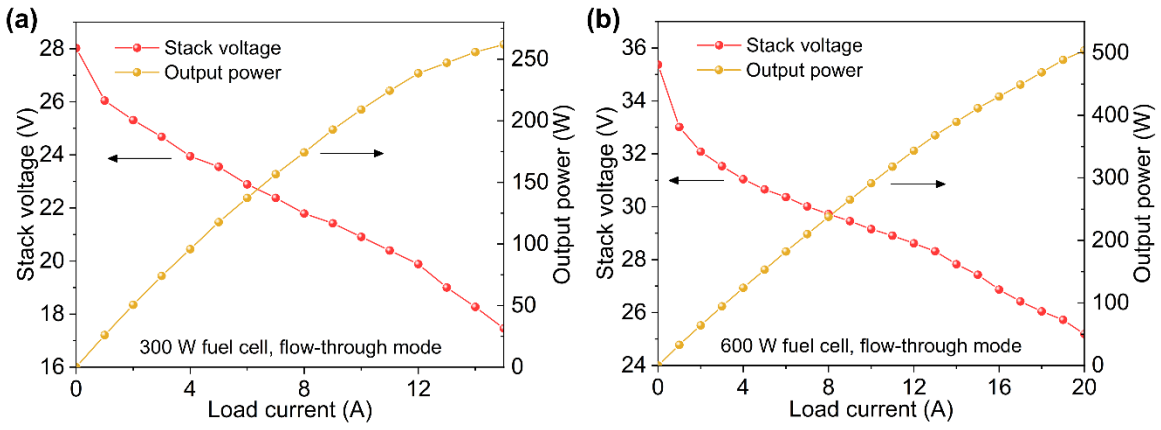

Fig. 6 Fuel cell performance with simulated cracked gas under flow-through mode for (a) full capacity of 300 W and (b) full capacity of 600 W.

3.6 Integration of the powertrain for electric golf cart

An integrated NH_3-powered fuel cell system was assembled based on the optimized catalyst, catalytic converter, gas purifier, and fuel cells. The integrated system is displayed in **Fig. S7**, and each component in the integration is shown in **Fig. S8**. To demonstrate the practical feasibility of this powerpack design, a powertrain (**Fig. S9**), including an NH_3-powered fuel cell and the motor system, has been configured on a golf cart and mediated by a 5 kWh battery energy storage with an energy management system to control and regulate energy flow between each unit to maximize the system efficiency. All components are assembled in series, enabling the H_2 produced from the NH_3 cracker and purified by the adsorption column to power the PEMFC. All tubes and vessels were sealed with 316 L

423 stainless steel to avoid corrosion and gas leakage. An overview of the setup is presented in
424 **Fig. 7**a.

425 For the current prototype, the Ni-HD catalyst material has been chosen as the NH_3
426 decomposition catalyst because of its low-cost and high activity at 600~700 ℃ operating
427 temperature. The post-reaction gas is predominantly a 75% H_2 and 25% N_2 mixture. A
428 trace amount of unreacted NH_3 is present, which can be efficiently removed by the zeolite
429 adsorbent. PEMFCs with the flow-through mode have been configured to accommodate
430 the cracked gas mixture to avoid N_2 building up and damaging the PEMFC. A buffer fuel
431 storage tank (4L) is installed to moderate any pressure changes caused by the flow-through
432 operation. The energy management system manages the fuel cell output, motor current,
433 battery's State of Charge (SOC), and the flow rate of the NH_3. An optimized energy control
434 to operate in the maximum power point tracking is developed.

435 System performance tests have been performed. The result is given in **Table 3** below.
436 Clearly, with an NH_3 flow rate of 3000 mL/min, the fuel cell can output a maximum power
437 of 255.3 W at 15 A under flow-through mode. When the flow rate was increased to 6000
438 mL/min, the output power can be enlarged to 491.8 W. Note that the power output was
439 restricted by the fuel cell used. We are confident that satisfactory energy efficiency can be
440 achieved with further system optimization, which will focus on the follow-up research
441 direction after this prototype. The figure of the assembled golf cart is shown in **Fig. 7**b, and
442 a short video recorded the running of the golf cart in practical application is given in **Movie**
443 **S1**. The vehicle has zero-carbon emissions and safer energy storage than conventional H_2
444 fuel cell vehicles. The hydrogen storage density of estimated scaled-up power system is
445 4.87 % (**Table S4**), exceeding the US Department of Energy (DOE)'s 2020 gravimetric

hydrogen capacity goals (4.5 wt%). Our team aims to scale up this powertrain system and adopt the finalized energy control technology to a minibus (15-30 kW) in late 2022. Relevant research is on-going now.

Table 3 Powerpack system performance testing result

Trial	Trial 1	Trial 2	Trial 3
Location	Golf cart	Golf cart	Golf cart
Catalyst	Fe-BZ	Ni-HD	Ni-HD
Activation gas	NH_3	NH_3	NH_3
Tube diameter (inch)	1”	1”	1”
Particle size (mesh)	45-60	45-60	45-60
NH_3 flow rate ($L \cdot min^{-1}$)	3	3	6
Furnace	FURN-M-1500	FURN-M-1500	FURN-M-1500
Temperature (°C)	700	700	700
Maximum output power of fuel cell (W)	246.5	255.3	491.8
Voltage at maximum power (V)	16.4	17.0	24.6
Current at maximum power (A)	15	15	20

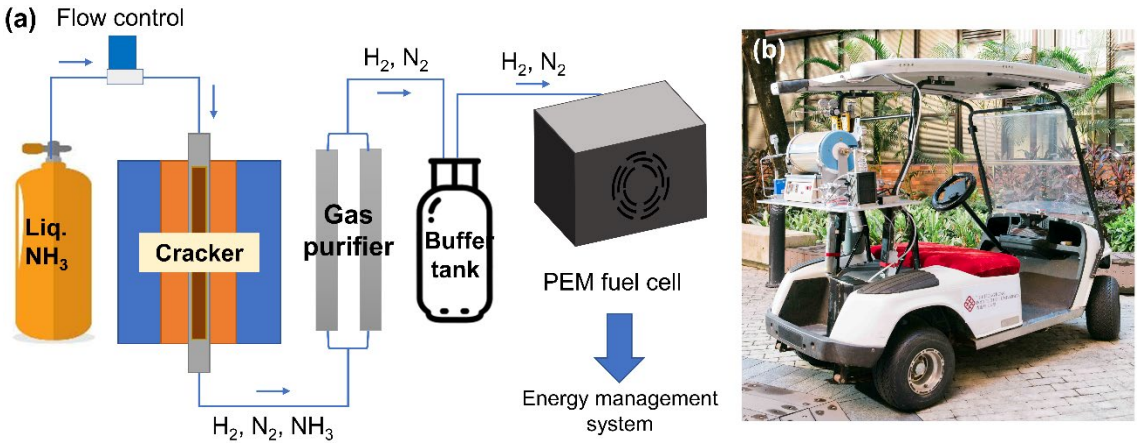

Fig. 7 (a) An overview of the target powerpack system, including NH_3 cracker, purification unit, fuel cell and energy management system. (b) Photograph of the assembled golf cart. Photo courtesy: PolyU CPA.

4. Conclusions

In summary, an NH_3-powered fuel cell electric golf cart system was firstly designed and optimized in this study. The system contains three main components: NH_3 cracker, fuel cell, and energy management unit. Four types of Ni and Fe-based catalysts were characterized, and the optimal Ru-modified commercial Ni catalyst demonstrated a > 99.9% NH_3 conversion at 600 ℃ at a GHSV of 3000 h^{-1}. To power the golf cart, NH_3 is stored in its liquid form inside a cylinder. It then goes through a cracker and is decomposed into N_2 and H_2 by the Ni-based catalyst. While > 99.9% of the NH_3 can be transformed into H_2 and N_2, the remainder is filtered out by a regenerable 13 X zeolite-based gas purifier. The decomposed gas mixture (75% H_2/25% N_2) is able to deliver a power of 503.8 W at 20 A and 25.2 V on a 600W fuel cell. The generated electricity was applied under a power point tracking to drive the golf cart with a 3kW motor drive. The demonstrated NH_3-powered

fuel cell prototype with an energy level of 17.5 kWh gives total system-specific energy of 379.4 Wh/kg. When equipped with 15 kg NH_3, the integrated power system is expected to meet the US Department of Energy's 2020 gravimetric hydrogen capacity target for onboard automotive hydrogen storage systems. Only N_2 and water are generated in the chemical processes of the system and emitted into the atmosphere, demonstrating that this power-generating technology is clean and carbon-free. Our proof-of-concept prototype represents a major leap in clean energy-powered electric vehicles and broadens the horizons for H_2 fuel applications.

Declaration of Competing Interest

The authors declare that they have no known competing financial interests or personal relationships that could have appeared to influence the work reported in this paper.

Acknowledgements

This work was financially supported by the Innovation and Technology Fund of Hong Kong (ITP/042/20AP). The authors would like to thank Prof Edman Tsang and Dr Simson Wu from the University of Oxford and Oxford Green Innotech for their participation in discussions and technical advice. The authors also gratefully acknowledge the support from Automotive Parts and Accessory Systems R&D Centre (APAS), and EV dynamics. The authors acknowledge PolyU CPA for the golf cart photo.

Appendix A. Supplementary data

Supplementary data to this article can be found online at https://doi.org/10.1016/j.cej.2022.XXXXXX.

Appendix B. Supplementary movie

Supplementary movie to this article can be found online at https://doi.org/10.1016/j.cej.2022.XXXXXX.

References

[1] J. Cha, Y.S. Jo, H. Jeong, J. Han, S.W. Nam, K.H. Song, C.W. Yoon, Ammonia as an efficient CO_x-free hydrogen carrier: Fundamentals and feasibility analyses for fuel cell applications, Appl. Energy 224 (2018) 194-204, https://doi.org/10.1016/j.apenergy.2018.04.100.

[2] F. Jiao, B. Xu, Electrochemical ammonia synthesis and ammonia fuel cells, Adv. Mater. 31(31) (2019) 1805173, https://doi.org/10.1002/adma.201805173.

[3] Y. Ishimoto, M. Voldsund, P. Nekså, S. Roussanaly, D. Berstad, S.O. Gardarsdottir, Large-scale production and transport of hydrogen from Norway to Europe and Japan: Value chain analysis and comparison of liquid hydrogen and ammonia as energy carriers, Int. J. Hydrog. Energy 45(58) (2020) 32865-32883, https://doi.org/10.1016/j.ijhydene.2020.09.017.

[4] M.S. Akhtar, J. Liu, Process Design and Techno-economic analysis of Hydrogen Production using Green Ammonia Imported from Australia-A Korea Case Study, Computer Aided Process Engineering 50 (2021) 141-146, https://doi.org/10.1016/B978-0-323-88506-5.50023-1.

[5] C.F. Guerra, L. Reyes-Bozo, E. Vyhmeister, M.J. Caparrós, J.L. Salazar, C. Clemente-Jul, Technical-economic analysis for a green ammonia production plant in Chile and its subsequent transport to Japan, Renew. Energ. 157 (2020) 404-414, https://doi.org/10.1016/j.renene.2020.05.041.

[6] M. Aziz, A.T. Wijayanta, A.B.D. Nandiyanto, Ammonia as effective hydrogen storage: A review on production, storage and utilization, Energies 13(12) (2020) 3062, https://doi.org/10.3390/en13123062.

[7] F. Chang, W. Gao, J. Guo, P. Chen, Emerging materials and methods toward ammonia-based energy storage and conversion, Adv. Mater. 33(50) (2021) 2005721, https://doi.org/10.1002/adma.202005721.

[8] F.B. Juangsa, A.R. Irhamna, M. Aziz, Production of ammonia as potential hydrogen carrier: Review on thermochemical and electrochemical processes, Int. J. Hydrog. Energy 46(27) (2021) 14455-14477, https://doi.org/10.1016/j.ijhydene.2021.01.214.

[9] D.R. MacFarlane, P.V. Cherepanov, J. Choi, B.H. Suryanto, R.Y. Hodgetts, J.M. Bakker, F.M.F. Vallana, A.N. Simonov, A roadmap to the ammonia economy, Joule 4(6) (2020) 1186-1205, https://doi.org/10.1016/j.joule.2020.04.004.

[10] S. Bajus, F. Agel, M. Kusche, N.N. Bhriain, P. Wasserscheid, Alkali hydroxide-modified Ru/γ-Al_2O_3 catalysts for ammonia decomposition, Appl. Catal. A 510 (2016) 189-195, https://doi.org/10.1016/j.apcata.2015.11.024.

[11] X. Ju, L. Liu, P. Yu, J. Guo, X. Zhang, T. He, G. Wu, P. Chen, Mesoporous Ru/MgO prepared by a deposition-precipitation method as highly active catalyst for producing CO_x-free hydrogen from ammonia decomposition, Appl. Catal. B 211 (2017) 167-175, https://doi.org/10.1016/j.apcatb.2017.04.043.

[12] R. Atsumi, R. Noda, H. Takagi, L. Vecchione, A. Di Carlo, Z. Del Prete, K. Kuramoto, Ammonia decomposition activity over Ni/SiO_2 catalysts with different pore diameters, Int. J. Hydrog. Energy 39(26) (2014) 13954-13961, https://doi.org/10.1016/j.ijhydene.2014.07.003.

[13] J. Zhang, J.-O. Müller, W. Zheng, D. Wang, D. Su, R. Schlögl, Individual Fe-Co alloy nanoparticles on carbon nanotubes: structural and catalytic properties, Nano Lett. 8(9) (2008) 2738-2743, https://doi.org/10.1021/nl8011984.

[14] L. Lin, L. Zhang, Y. Luo, J. Luo, C. Chen, L. Jiang, Highly-integrated and cost-efficient ammonia-fueled fuel cell system for efficient power generation: a comprehensive system optimization and techno-economic analysis, Energy Convers. Manag. 251 (2022) 114917, https://doi.org/10.1016/j.enconman.2021.114917.

[15] C. Makhloufi, N. Kezibri, Large-scale decomposition of green ammonia for pure hydrogen production, Int. J. Hydrog. Energy 46(70) (2021) 34777-34787, https://doi.org/10.1016/j.ijhydene.2021.07.188.

[16] Z. Chen, H. Wang, N.Q. Su, S. Duan, T. Shen, X. Xu, Beyond mean-field microkinetics: toward accurate and efficient theoretical modeling in heterogeneous catalysis, ACS Catal. 8(7) (2018) 5816-5826, https://doi.org/10.1021/acscatal.8b00943.

555 [17] S. Mukherjee, S.V. Devaguptapu, A. Sviripa, C.R. Lund, G. Wu, Low-temperature
556 ammonia decomposition catalysts for hydrogen generation, Appl. Catal. B 226 (2018) 162-
557 181, https://doi.org/10.1016/j.apcatb.2017.12.039.
558 [18] D.A. Hansgen, D.G. Vlachos, J.G. Chen, Using first principles to predict bimetallic
559 catalysts for the ammonia decomposition reaction, Nat. Chem. 2(6) (2010) 484-489,
560 https://doi.org/10.1038/nchem.626.
561 [19] C. Chen, K. Wu, H. Ren, C. Zhou, Y. Luo, L. Lin, C. Au, L. Jiang, Ru-based catalysts
562 for ammonia decomposition: a mini-review, Energy Fuels 35(15) (2021) 11693-11706,
563 https://doi.org/10.1021/acs.energyfuels.1c01261.
564 [20] T.A. Le, Y. Kim, H.W. Kim, S.-U. Lee, J.-R. Kim, T.-W. Kim, Y.-J. Lee, H.-J. Chae,
565 Ru-supported lanthania-ceria composite as an efficient catalyst for CO_x-free H_2 production
566 from ammonia decomposition, Appl. Catal. B 285 (2021) 119831,
567 https://doi.org/10.1016/j.apcatb.2020.119831.
568 [21] K.M. Bui, J.-I. Iwata, Y. Kangawa, K. Shiraishi, Y. Shigeta, A. Oshiyama, Reaction
569 pathway of surface-catalyzed ammonia decomposition and nitrogen incorporation in
570 epitaxial growth of gallium nitride, J. Phys. Chem. C 122(43) (2018) 24665-24671,
571 https://doi.org/10.1021/acs.jpcc.8b05682.
572 [22] L. Shen, X. Li, D. Lindberg, P. Taskinen, Tungsten extractive metallurgy: A review
573 of processes and their challenges for sustainability, Miner. Eng. 142 (2019) 105934,
574 https://doi.org/10.1016/j.mineng.2019.105934.
575 [23] C. Zamfirescu, I. Dincer, Ammonia as a green fuel and hydrogen source for vehicular
576 applications, Fuel Process. Technol. 90(5) (2009) 729-737,
577 https://doi.org/10.1016/j.fuproc.2009.02.004.

578 [24] K.E. Lamb, M.D. Dolan, D.F. Kennedy, Ammonia for hydrogen storage; A review of
579 catalytic ammonia decomposition and hydrogen separation and purification, Int. J. Hydrog.
580 Energy 44(7) (2019) 3580-3593, https://doi.org/10.1016/j.ijhydene.2018.12.024.
581 [25] J. Zhu, S.S. Araya, X. Cui, S.L. Sahlin, S.K. Kær, Modeling and design of a multi-
582 tubular packed-bed reactor for methanol steam reforming over a $Cu/ZnO/Al_2O_3$ catalyst,
583 Energies 13(3) (2020) 610, https://doi.org/10.3390/en13030610.
584 [26] H. Miyaoka, H. Miyaoka, T. Ichikawa, T. Ichikawa, Y. Kojima, Highly purified
585 hydrogen production from ammonia for PEM fuel cell, Int. J. Hydrog. Energy 43(31) (2018)
586 14486-14492, https://doi.org/10.1016/j.ijhydene.2018.06.065.
587 [27] H.J. Soto, W.-k. Lee, J. Van Zee, M. Murthy, Effect of transient ammonia
588 concentrations on PEMFC performance, Electrochem. Solid-State Lett. 6(7) (2003) A133,
589 https://doi.org/10.1149/1.1574651.
590 [28] R. Halseid, P.J. Vie, R. Tunold, Effect of ammonia on the performance of polymer
591 electrolyte membrane fuel cells, J. Power Sources 154(2) (2006) 343-350,
592 https://doi.org/10.1016/j.jpowsour.2005.10.011.
593 [29] P.M. Ndegwa, V.K. Vaddella, A. Hristov, H. Joo, Measuring concentrations of
594 ammonia in ambient air or exhaust air stream using acid traps, J. Environ. Qual. 38(2)
595 (2009) 647-653, https://doi.org/10.2134/jeq2008.0211.
596 [30] A.A. Halim, H.A. Aziz, M.A.M. Johari, K.S. Ariffin, Comparison study of ammonia
597 and COD adsorption on zeolite, activated carbon and composite materials in landfill
598 leachate treatment, Desalination 262(1-3) (2010) 31-35,
599 https://doi.org/10.1016/j.desal.2010.05.036.

600 [31] C.C. Rodrigues, D. de Moraes Jr, S.W. Da Nobrega, M.G. Barboza, Ammonia
601 adsorption in a fixed bed of activated carbon, Bioresour. Technol. 98(4) (2007) 886-891,
602 https://doi.org/10.1016/j.biortech.2006.03.024.
603 [32] D. Saha, S. Deng, Ammonia adsorption and its effects on framework stability of MOF-
604 5 and MOF-177, J. Colloid Interface Sci. 348(2) (2010) 615-620,
605 https://doi.org/10.1016/j.jcis.2010.04.078.
606 [33] C. Petit, C. Karwacki, G. Peterson, T.J. Bandosz, Interactions of ammonia with the
607 surface of microporous carbon impregnated with transition metal chlorides, J. Phys. Chem.
608 C 111(34) (2007) 12705-12714, https://doi.org/10.1021/jp072066n.
609 [34] W. Ouyang, S. Zheng, C. Wu, X. Hu, R. Chen, L. Zhuo, Z. Wang, Dynamic ammonia
610 adsorption by FAU zeolites to below 0.1 ppm for hydrogen energy applications, Int. J.
611 Hydrog. Energy 46(64) (2021) 32559-32569,
612 https://doi.org/10.1016/j.ijhydene.2021.07.107.
613 [35] J. Yu, Z. Jiang, M. Hou, D. Liang, Y. Xiao, M. Dou, Z. Shao, B. Yi, Analysis of the
614 behavior and degradation in proton exchange membrane fuel cells with a dead-ended anode,
615 J. Power Sources 246 (2014) 90-94, https://doi.org/10.1016/j.jpowsour.2013.06.163.
616 [36] J.B. Siegel, S.V. Bohac, A.G. Stefanopoulou, S. Yesilyurt, Nitrogen front evolution
617 in purged polymer electrolyte membrane fuel cell with dead-ended anode, J. Electrochem.
618 Soc. 157(7) (2010) B1081, https://doi.org/10.1149/1.3425743.

619